



**HAL**  
open science

# A combined experimental and theoretical study on the synthesis, spectroscopic characterization of Magnesium(II) porphyrin complex with DMAP axial ligand and antifungal activity

S. Jabli, M. Chaabene, T. Roisnel, F. Molton, F. Loiseau, P. Jéhan, R.B. Chaabane, H. Nasri

## ► To cite this version:

S. Jabli, M. Chaabene, T. Roisnel, F. Molton, F. Loiseau, et al.. A combined experimental and theoretical study on the synthesis, spectroscopic characterization of Magnesium(II) porphyrin complex with DMAP axial ligand and antifungal activity. *Journal of Molecular Structure*, 2022, 1267, pp.133559. 10.1016/j.molstruc.2022.133559 . hal-03780208v2

**HAL Id: hal-03780208**

**<https://hal.science/hal-03780208v2>**

Submitted on 20 Sep 2022

**HAL** is a multi-disciplinary open access archive for the deposit and dissemination of scientific research documents, whether they are published or not. The documents may come from teaching and research institutions in France or abroad, or from public or private research centers.

L'archive ouverte pluridisciplinaire **HAL**, est destinée au dépôt et à la diffusion de documents scientifiques de niveau recherche, publiés ou non, émanant des établissements d'enseignement et de recherche français ou étrangers, des laboratoires publics ou privés.

**Highlights**

- Synthesis of the (DMAP)[*méso*-tetra(para-tolylphenyl)porphyrinato]magnésium complex (**I**).
- <sup>1</sup>H NMR, IR, UV-Visible, Fluorescence and mass spectroscopy investigations of (**I**).
- Single crystal X-ray molecular structure of (**I**) is reported.
- Cyclic voltammetry data and DFT calculations on complex are reported.
- Antifungal activities are tested on H<sub>2</sub>TTP, the [MgTTP], and the complex (**I**).

Journal Pre-proof

# A combined experimental and theoretical study on the Synthesis, Spectroscopic Characterization of Magnesium(II) Porphyrin Complex with DMAP axial ligand and antifungal activity

Souhir Jabli <sup>a,\*</sup>, Marwa Chaabene <sup>b,\*</sup>, Thierry Roisnel <sup>c</sup>, Florian Molton <sup>d</sup>, Frédérique Loiseau <sup>d</sup>, Philippe Jehan <sup>e</sup>, Rafik Ben Chaabane <sup>b</sup>, Habib Nasri <sup>a</sup>

<sup>a</sup>: University of Monastir, Laboratory of Physical Chemistry of Materials (LR01ES19), Faculty of Sciences of Monastir, Avenue de l'environnement, 5019 Monastir, Tunisia.

<sup>b</sup>: University of Monastir, Laboratory of advanced materials and interfaces (LIMA), Faculty of Sciences of Monastir, Monastir, 5019, Tunisia.

<sup>c</sup>: Centre de Diffractométrie X, Institut des Sciences Chimiques de Rennes, UMR 6226, CNRS-Université de Rennes 1, Campus de Beaulieu, 35042 Rennes Cedex, France.

<sup>d</sup>: Département de Chimie Moléculaire, 301 rue de la Chimie, Université Grenoble Alpes, CS 40700, 38058 Grenoble, Cedex 9, France.

<sup>e</sup>: Centre Régional de Mesures Physiques de l'Ouest (CRMPO) ScanMAT UMS 2001 CNRS, Université de Rennes 1, Campus de Beaulieu, 35042 RENNES Cedex, France

## Abstract

We report in the present paper the synthesis, the spectroscopic, structural, and electrochemical properties of a new magnesium(II) coordination compound namely the bis(4-dimethylaminopyridine)[*meso*-tetra(*p*-tolyl)porphyrinato]magnesium(II) dichloromethane disolvate complex with the formula [Mg(TTP)(DMAP)<sub>2</sub>] $\cdot$ 2CH<sub>2</sub>Cl<sub>2</sub> (**I**). This species crystallizes in the triclinic crystal system with the centrosymmetric space group *P*-1. The crystal lattice of (**I**) is stabilized by C–H $\cdots$ Cg (Cg is the centroid of a phenyl ring) and C–H $\cdots$ Cl intermolecular interactions. Further insights on these weak intermolecular contacts are provided by the Hirshfeld surface analysis. This new Mg(II) porphyrin species was characterized by <sup>1</sup>H NMR, IR, fluorescence, UV/Vis spectroscopy and ESI-HRMS mass spectrometry. A cyclic voltammetry investigation of this new metalloporphyrin was also reported. Furthermore, the bioactivity of the H<sub>2</sub>TTP free base porphyrin, the [Mg(TTP)] starting material and [Mg(TTP)(DMAP)<sub>2</sub>] $\cdot$ 2CH<sub>2</sub>Cl<sub>2</sub> (**I**) was evaluated *in vitro*, by examining their inhibitory effect against three strains of *Candida* viz. *C. albicans*, *C. glabrata* and *C. tropicalis* with MIC values in the range 2.5 to 10  $\mu$ g.mL<sup>-1</sup>. The screening of the susceptibility of *M. canis* and *T. rubrum* clinical strains on the three porphyrinic derivatives is also reported.

---

\*Corresponding author: [souhir.jabli@gmail.com](mailto:souhir.jabli@gmail.com) and [marwachaaben0@gmail.com](mailto:marwachaaben0@gmail.com)

**Keywords:** Magnesium(II) porphyrin complex; DFT calculations; X-ray molecular structure; UV/Vis; Cyclic voltammetry.

## 1. Introduction

Metalloporphyrins have been extensively studied since the early 1960s. This great attention to these coordination compounds is mainly related to the fact that they were investigated as synthetic models for hemoproteins such as myoglobin, hemoglobin, cytochromes c and cytochromes P450. Over the last three decades, the field of use of porphyrin compounds has spanned disciplines ranging from chemistry, biology, physics, electronics, pharmacy, and medicine [1–3]. Moreover, due to their remarkable and quite flexible photophysical properties, they have been extensively developed for various bioapplications. The most successful of which is the use of these species in cancer treatment [4] and as chemical sensors [5]. Currently, porphyrins and metalloporphyrins are used in many technical applications including, catalysts [6], supramolecular chemistry [7], photocatalysts [8], semiconductors [9] and photosensitizers in photodynamic therapy, because of their excellent light-harvesting capability, long excited-state lifetime, and good stability [10].

The magnesium porphyrin complexes are strongly fluorescent, compared to those of open-shell paramagnetic metal ions such as manganese and fer. Diamagnetic  $Zn^{2+}$  and  $Mg^{2+}$  metalloporphyrins display quite similar absorption and emission properties. However, magnesium porphyrins exhibit a higher fluorescence quantum yields and longer excited-state lifetimes compared to those of zinc porphyrins [10]. Zinc porphyrins have been extensively studied, mainly because the insertion of  $Zn^{2+}$  ion into the porphyrin core is very easy compared to that of  $Mg^{2+}$  ion. Notably, in all reported X-ray molecular structures porphyrin complexes magnesium centers are pentacoordinated and hexacoordinated and up to date, 80 structures are present in the Cambridge Structural Database compared to 1461 reported zinc(II) metalloporphyrin structures (CSD Version 5.42, last update April 2021).

On the other hand, the last decade has witnessed intense research projects devoted to the antioxidant, antibacterial and antifungal activities of porphyrin species *in vitro* [11–16] and many studies demonstrated that porphyrins are effective against viruses and yeasts [17,18]. It should also be noted that our research group has published in recent years a number of works concerning the use of magnesium porphyrin complexes as antifungal and antibacterial agents [19,20].

As a continuation of our investigation of magnesium porphyrin complexes, a new coordination compound has been synthesized entitled: bis(4-(dimethylamino)pyridine)[*meso*-tetra(tolylphenyl)porphyrinato]magnesium(II) dichloromethane disolvate with formula  $[Mg(TTP)(DMAP)_2] \cdot 2CH_2Cl_2$  (**I**) where TTP is the *meso* -tetra(tolylphenyl)porphyrinato and

DMAP is the 4-(dimethylamino)pyridine. This Mg(II) porphyrin derivative was characterized by single crystal X-ray investigation and by Hirshfeld surfaces analysis.  $^1\text{H}$  NMR, IR, fluorescence spectroscopy and UV/Vis methods were reported to confirm the structure of this Mg(II) coordination compound. Complex (**I**) was further investigated by MALDI-TOF mass spectrometry and cyclic voltammetry. With recent progress in developing powerful software for the useful approximate functionals in the density functional theory, the DFT calculations [21–22] have become a popular approach for the theoretical studies of molecular structure, chemical reactivity, phosphorescence, force fields and infrared (IR) absorption spectra. In order to better understand the molecular structure of the complex (**I**), theoretical structural analysis was performed, and the chemical reactivity behaviors were investigated. Furthermore, the antifungal activities of the [Mg(TTP)] starting material and complex (**I**) were also performed.

## 2. Experimental Section

### 2.1. Synthesis

All reagents employed were commercially available and were used as received without further purification.

#### 2.1.1. Synthesis of $\text{H}_2\text{TTP}$ and [Mg(TTP)]

The *meso*-tetratolylporphyrin ( $\text{H}_2\text{TTP}$ ) was prepared by using the Alder and Longo method [23] and the [Mg(TTP)] starting material was prepared as reported in the literature method [24–26].

The  $\text{H}_2\text{TTP}$  free base porphyrin 0.5 g (0.74 mmol) was dissolved in 40 mL of dichloromethane then 1.35 g of  $\text{MgBr}_2\text{O}(\text{Et})_2$  (5.25 mmol) and 2 mL (14 mmol) of triethylamine were added. The mixture was stirred under  $\text{N}_2$  atmosphere at room temperature for 1h. The [Mg(TTP)] complex precipitated after the addition of 40 mL of dichloromethane then the mixture was washed with distilled water. After decantation, 100 g of  $\text{Na}_2\text{SO}_4$  was added to the organic phase then stirred for 30 min. The solvent was removed and [Mg(TTP)] was obtained by precipitation in a dichloromethane - n-hexane mixture with a yield of 94% (470 mg).

#### 2.1.2. Synthesis of [Mg<sup>II</sup>(TTP)(DMAP)<sub>2</sub>].2CH<sub>2</sub>Cl<sub>2</sub> (**I**)

[Mg(TTP)] (30 mg, 0.043 mmol) and 4-dimethylaminopyridine (DMAP) (90 mg, 0.73 mmol) were dissolved in 5 mL of dichloromethane and stirred at room temperature overnight. The color of the solution changes to green blue. The obtained compound crystallizes by slow diffusion of n-hexane through the dichloromethane solution to give after one week a dark-blue

crystal (63 mg, 90% yield).

Elemental analysis calcd (%) for  $C_{64}H_{60}Cl_4MgN_8$ , C 79.61, H 6.26, N 11.61; found: C 78.92, H 6.08, N 11.23 UV/Vis [ $CH_2Cl_2$ ]:  $\lambda_{max}$  : 427, 566, 606 nm.  $^1H$  RMN (500 MHz,  $CDCl_3$ )  $\delta$  (ppm) : 8.85 (H $\beta$ -pyrrol), 8.10 (H $_{o,o}$  Porph), 7.53 (H $_{m,m}$  Porph), 7.67 (H $_{L,o}$  4-DMAP), 7.25 (H $_{L,m}$  DMAP), 2.62 (CH $_3$ -porphyrin), 2.70 (CH $_3$ -DMAP). IR (solid,  $cm^{-1}$ ): 3025 [ $\nu$ (CH)-DMAP] , 2808-2920 [ $\nu$ (CH) porphyrin], 1499 [ $\nu$ (C=N,C=C) porphyrin], 996 [ $\delta$ (CCH) porphyrin]; MS (ESI $^+$  HRMS,  $CH_2Cl_2$ ):  $m/z$  = 692.27849 [ $Mg(TTP)^+$ ] trouvé 692.2782,  $m/z$  = 895.45511 [ $Mg(TTP)(DMAP)_2+H^+$ ] trouvé 937.4547.

## 2.2. X-ray structure determination

Single crystals of  $[Mg(TTP)(DMAP)_2] \cdot 2CH_2Cl_2$  (**I**) with dimensions of 0.62 mm x 0.58 mm x 0.30 mm were obtained by slow diffusion of *n*-hexane into a dichloromethane solution of (**I**). Crystal evaluation and data collection were performed on a D8 VENTURE Bruker AXS diffractometer equipped with a CCD area detector with Mo Ka radiation ( $\lambda = 0.71073 \text{ \AA}$ ). The crystals were kept at 150 (2) K during data collection. The data were scaled and corrected for absorption correction using SADABS-2004/1 (Bruker, 2004) [27]. The structure was solved by direct methods using SIR-2004 [28] and refined by using the SHELXL-2014 program [29]. The geometrical calculations were carried out using the program PLATON [30] and the molecular and packing diagrams were generated using the software MERCURY [31]. The crystallographic data and structural refinement details of (**I**) are shown in Table 1. Selected bond lengths and angles for the compound are listed in Table 2.

Table 1. Crystal data and structural refinement for  $[Mg(TTP)(DMAP)_2] \cdot 2CH_2Cl_2$  (**I**).

Formula	$C_{64}H_{60}Cl_4MgN_8$
M.W.	1107.31 g/mol
Crystal System	triclinic
Crystal	<i>P</i> -1
<i>a</i> (Å)	10.7650 (11)
<i>b</i> (Å)	10.8800 (11)
<i>c</i> (Å)	13.1590 (13)
$\alpha$ (°)	75.028 (3)
$\beta$ (°)	87.747 (3)
$\gamma$ (°)	68.827 (4)
<i>V</i> (Å $^3$ )	1385.9 (2)
<i>Z</i>	2
$\rho_{calc.}$ / g.cm $^{-3}$	1.327
$\mu$ / mm $^{-1}$	0.275
<i>F</i> (000)	580

Crystal size (mm <sup>3</sup> )	0.62 x 0.58 x 0.30
Crystal Color	purple
Crystal Shape	prism
T(K)	150 (2)
$\theta_{min} - \theta_{max}$ (°)	2.942 – 27.000
Limiting indices	-9 ≤ h ≤ 13, -11 ≤ k ≤ 14, -17 ≤ l ≤ 16
$R(int)$	0.0290
Total/Unique data	17777/6291
Observed data [ $I_o > 2\sigma(F_o)$ ]	13088
Parameters/Rest	6291/353
S [Goodness of fit]	1.027
$R_1^a, wR_2^b$ [ $F_o > 4\sigma(F_o)$ ]	$R_1 = 0.0443, wR_2 = 0.1119$
$wR_2^b$ [all data]	$R_1 = 0.0570, wR_2 = 0.1207$
Min./max. res. (eÅ <sup>-3</sup> )	0.338 /-0.528
CCDC	2176543

<sup>a</sup>:  $R_1 = \frac{\sum ||F_o| - |F_c||}{\sum |F_o|}$ , <sup>b</sup>:  $wR_2 = \left\{ \frac{\sum [w(|F_o|^2 - |F_c|^2)^2]}{\sum [w(|F_o|^2)^2]} \right\}^{1/2}$ .

Table 2. Selected bond lengths (Å) and angles (°) of (I).

<i>Magnesium coordination polyhedron</i>					
	(Å) <sub>Exp</sub>	(Å) <sub>Theo</sub>		(°) <sub>Exp</sub>	(°) <sub>Theo</sub>
Mg-N <sub>1</sub>	2.080	2.090	N <sub>1</sub> -Mg-N <sub>2</sub>	89.48	88.35
Mg-N <sub>2</sub>	2.060	2.090	N <sub>1</sub> -Mg-N <sub>31</sub>	86.60	88.32
Mg-N <sub>31</sub>	2.316	2.111	N <sub>2</sub> -Mg-N <sub>31</sub>	91.66	88.37
<i>4-dimethylaminopyridine (DMAP) Axial ligand</i>					
	(Å) <sub>Exp</sub>	(Å) <sub>Theo</sub>		(°) <sub>Exp</sub>	(°) <sub>Theo</sub>
N <sub>31</sub> -C <sub>36</sub>	1.343	1.342	Mg-N <sub>31</sub> -C <sub>32</sub>	123.04	120.66
N <sub>31</sub> -C <sub>32</sub>	1.346	1.341	Mg-N <sub>31</sub> -C <sub>36</sub>	122.26	122.57
N <sub>37</sub> -C <sub>38</sub>	1.358	1.374	C <sub>32</sub> -N <sub>31</sub> -C <sub>36</sub>	114.38	116.72
N <sub>37</sub> -C <sub>39</sub>	1.455	1.454	C <sub>34</sub> -N <sub>37</sub> -C <sub>39</sub>	120.37	119.84

### 2.3. Quantum chemical calculation

B3LYP [32] with the empirical dispersion correction D3 of Grimme *et al.*, [33] has been evaluated. The B3LYP-D3 functional with 6-311G (d, p) basis set has been selected to optimize the geometries of synthesized compounds. It was found to provide a good compromise between accuracy and computation time for structure optimizations. Furthermore, we noticed that B3LYP-D3 gave the lowest gap energy and the closest to the experimental results when compared to the other functional ones. This program was commonly used in literature [34-36] where it provides an efficient and robust basis for III-V semiconductor computations [37].

The <sup>1</sup>H calculations utilized the Gauge-Independent Atomic Orbital (GIAO) [38] method. In all cases <sup>1</sup>H for the test molecules were corrected with chemical shift (δ/ppm) relative to simulated values for tetramethylsilane (TMS), computed at the same level. Calculations of vibrational IR

frequencies have been carried out with the same method as geometry optimization in gas phase. It has been confirmed that these structures correspond to the characteristics of the local minimum by the absence of an imaginary mode. The photoluminescence (PL) spectra have been derived from CIS/TD-DFT calculations [39]. UV/Vis spectra were performed at the time dependent density functional theory (TD-DFT) with CAM-B3LYP/6-311 G (d, p) level of theory [40-41] which is used to calculate energies oscillator and the absorption wavelengths.

Moreover, by using the energies of the highest occupied molecular orbital (HOMO) ( $E_{HOMO}$ ) and of the lowest unoccupied molecular orbital (LUMO) ( $E_{LUMO}$ ), different global reactivity parameters have been determined such as electronic gap energy ( $E_g$ ), chemical potential ( $\mu$ ), global hardness ( $\eta$ ), electrophilicity ( $\omega$ ) and global softness ( $\sigma$ ). All of the calculations were performed using Gaussian 09 quantum chemistry package [42] and the visualizations were performed by the graphical interfaces Gaussview [36].

## **2.4. Antifungal activity**

### **2.4.1 Fungal strain and culture conditions**

The antifungal effect of the three porphyrins species was explored against yeasts from *Candida* genus from the American Type Culture Collection : *Candida albicans* (ATCC 90028), *Candida glabrata* (ATCC 64677) and *Candida tropicalis* (ATCC 66029) and two genus of dermatophytes : *Trichophyton rubrum* (MS 7793.1) and *Microsporum canis* (MS 8972), identified from clinical isolates by the professional team in the laboratory of parasitology and mycology of the teaching hospital Fattouma Bourguiba (Monastir-Tunisia). Before each antifungal assay, mycosis strains were maintained in culture on Sabouraud dextrose agar (Biolife) plates, at 30°C during 48 hours for *Candida* spp. and seven days for the dermatophytes.

### **2.4.2. Anticandidal activity**

#### **2.4.2.1. Determination of minimum inhibitory concentration (MIC) on *Candida* spp.**

The determination of Minimum Inhibitory Concentration (MIC) of the three porphyrin compounds on the fungal strains was processed as described by Hrichi *et al.* [43] using the microdilution method on flat bottom 96-well plates in the presence of Resazurin viability indicator. Briefly, the porphyrins were solubilized in dimethyl sulfoxide (DMSO) (m/v), and then adjusted in RPMI 1640 (PAN), supplemented by 2% glucose. Two hundred microliters of the porphyrin solutions were added into the first well of each line of the 96-well plate, then 100



$\mu\text{L}$  of RPMI 1640-2% glucose were dispensed in the remaining wells. A two fold serial dilution was applied from the first into tenth consecutive wells to obtain concentrations ranging from 10 to  $78.10^{-2} \text{ mg.mL}^{-1}$ . Thereafter, each well was inoculated with 90  $\mu\text{L}$  of inoculum adjusted to  $1-2.5.10^5 \text{ UFC mL}^{-1}$ . Then, 10  $\mu\text{L}$  of resazurin indicator solution was added to a final volume of 200  $\mu\text{L}$  per well. Positive (RPMI 1640-2% glucose with inoculum) and negative (RPMI 1640-2% glucose) control growth were included in all trials. Plates were then incubated at  $37^\circ\text{C}$  for 24 hours. Each experiment was run in triplicate. After incubation, the blue color indicates inhibition of growth, pink color indicates reduction of resorufin, and then persistence of strains. The lowest concentration which inhibited the visual growth was recorded as MIC.

#### **2.4.2.2. Determination of minimum fungicide concentration (MFC) on *Candida* spp.**

To determine the minimum fungicide concentration (MFC), 10  $\mu\text{L}$  of each blue-stained well was loop spread onto Sabouraud Dextrose Agar (SDA) plates and incubated at the corresponding temperature. The concentration that induces no visible colonies or revealed three colonies or less to obtain approximately 99 to 99.5% killing growth after subsequent 7 days incubation was accepted as MFC.

#### **2.4.3. Anti-dermatophytic activity**

##### **2.4.3.1. Anti-dermatophytic potential Screening**

The *in vitro* anti-dermatophytic activity of porphyrins was screened by the agar incorporation technique in 24-well plates [43]. After a primer dissolution in DMSO (m/v), each porphyrin candidate was dissolved in 1 mL of SDA medium to obtain a final concentration  $10 \text{ mg.mL}^{-1}$ . Well without substance was used as a negative control to monitor the growth of dermatophytes under normal conditions. Mycelial agar discs (2 mm) cut from an actively 7 days' old growing culture of dermatophytes, were bored in the center of each petri dish. Each treatment consisted of triplicates. The percentage of growth inhibition of porphyrin was calculated by the formula  $\% \text{ I inhibition} = [\text{growth in control} - \text{growth in sample} / \text{growth in control}] \times 100$ .

##### **2.4.3.2. Evaluation of the mycelial radial growth of dermatophytes**

Three concentrations ( $5 \text{ mg.mL}^{-1}$ ,  $2.5 \text{ mg.mL}^{-1}$  and  $1.25 \text{ mg.mL}^{-1}$ ) of porphyrins with proven antifungal potential were incorporated in a final volume of 3 mL of SDA medium. A petri dish without substance was used as a negative control to monitor the growth of dermatophytes under normal conditions. A mycelial agar discs (2 mm) cut from the actively growing culture of 7 days old, were bored in the center of each petri dish. Each treatment consisted of triplicates.

Petri dishes were sealed with parafilm to avoid dehydration. In that method radical growth was three-time interval measured for each concentration.

The percentage of growth inhibition of porphyrin was calculated by the formula:

$$\% \text{ I inhibition} = [\text{growth in control} - \text{growth in sample} / \text{growth in control}] \times 100.$$

### 3. Results and Discussion

#### 3.1. X-ray Structure of complex (I)

In Table 1 are summarized the crystal data and structure refinement parameters of  $[\text{Mg}(\text{TTP})(\text{DMAP})_2] \cdot 2\text{CH}_2\text{Cl}_2$  (**I**). This new magnesium(II) metalloporphyrin crystallizes in the triclinic group system with *P*-1 space group and two molecule formula by unit cell (*Z*). The unit cell parameters are  $a = 10.7650$  (11) Å,  $b = 10.8800$  (11) Å,  $c = 13.1590$  (13) Å,  $\alpha = 75.028$  (3)°,  $\beta = 87.747$  (3)°,  $\gamma = 68.827$  (4)°. The asymmetric unit of (**I**) is made by half a molecule of  $[\text{Mg}(\text{TTP})(\text{DMAP})_2]$  and one dichloromethane solvent molecule. Figure 1 is an ORTEP drawing of  $[\text{Mg}(\text{TTP})(\text{DMAP})_2]$ .

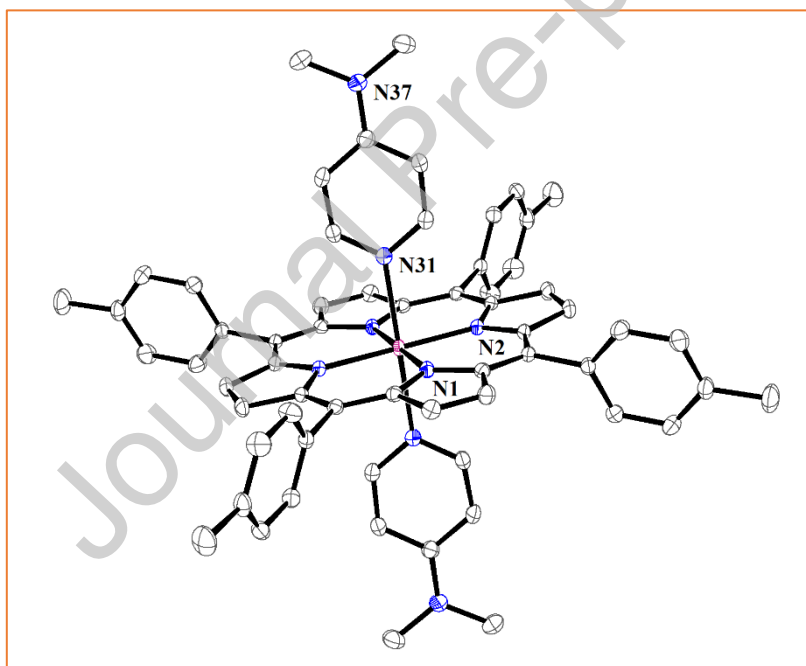


Fig. 1. Ortep drawing of  $[\text{Mg}(\text{TMPP})(\text{DMAP})_2]$  with thermal ellipsoids drawn at 50% probability. The hydrogen atoms are removed for clarity

The coordination geometry around the Mg(II) center metal ion in (**I**) is octahedral, where the four nitrogen atoms of the pyrrole rings of the TTP moiety occupy the equatorial positions and the N atoms of the pyridyl group of the trans DMAP axial ligands occupy the apical positions.

The theoretical molecular geometries of  $\text{H}_2\text{TTP}$ ,  $[\text{Mg}(\text{TTP})]$  and  $[\text{Mg}(\text{TTP})(\text{DMAP})_2]$  were shown in Figure 2. They were optimized at B3LYP-D3/6-311 G (d, p) level. Selected bond lengths ( $\text{\AA}$ ) and bond angles ( $^\circ$ ) of the complex (**I**) are listed in Table 2 and compared to those found with X-ray experimental study. They were simulated with the assumption that the solvent used for crystallization is dichloromethane. As shown in this latter figure, The Mg–N(DMAP) distance value of (**I**) is 2.317(2)  $\text{\AA}$  and 2.111  $\text{\AA}$  for the experimental and theoretical values, respectively. This result seems in agreement with Mg–N bond length of  $[\text{Mg}(\text{TPP})(4\text{-pic})_2]$  and  $[\text{Mg}(\text{TPBP})(4,4'\text{-bpy})_2]$ , where the Mg–N<sub>L</sub> (L: axial ligand) bonds are 2.345  $\text{\AA}$  and 2.320  $\text{\AA}$  respectively [44,45] which indicates the strong coordination bond of the DMAP ligand to the  $[\text{Mg}(\text{TTP})]$  moiety.

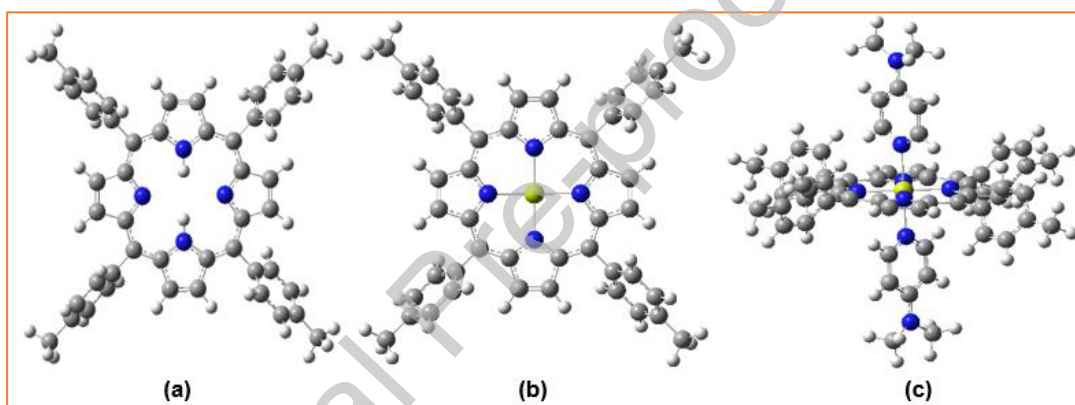


Fig. 2. Optimized geometries of the  $\text{H}_2\text{TTP}$  (a),  $[\text{Mg}(\text{TTP})]$  (b) and complex (**I**) (c) computed at the B3LYP-D3/6–311 G (d, p) level in dichloromethane solvent.

A part of the packing diagram of (**I**) is illustrated in Figure S1. The cohesion of the crystal packing for this TTP-Mg-DMAP species is stabilized by non-conventional C–H...Cl and C–H...Cg intermolecular interactions involving the pyrrole and phenyl rings of the porphyrins (Table S1, Figure 3, Figure S2) (Cg = the centroid of a pyrrole or a phenyl ring). Indeed, as shown in Figure 3 the carbon atom C32 from coordinated DMAP molecule is H-bonded to the centroid of the pyrrole of the *meso*-arylporphyrin with a C32–H32...Cg2 (Cg2 is the centroid of N2–C6–C7–C8–C9 pyrrole ring) distance of 3.169 (2)  $\text{\AA}$  and the carbon atom C101 of the dichloromethane molecule is weakly H-bonded to the centroid of the phenyl ring of the TTP porphyrinate with a C101–H10B–Cg5 distance of 3.623(3)  $\text{\AA}$  (Cg5 is the centroid of C21–C22–C23–C24–C25–C26). On the other hand, neighboring  $[\text{Mg}(\text{TTP})(\text{DMAP})_2]$  molecules are linked

one to the other by the intermolecular interaction C27–H27C...Cg21 where Cg21 is the centroid of N31-C32-C33-C34-C35-C36 of the phenyl of the DMAP axial ligand.

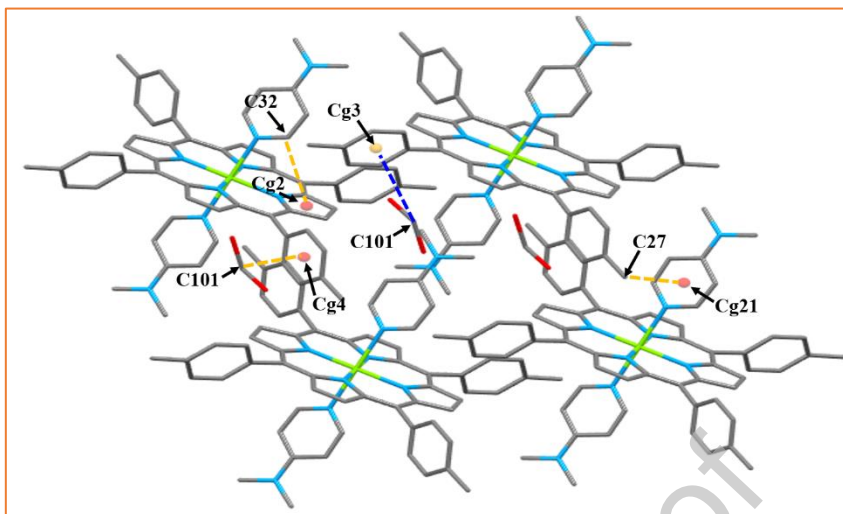


Fig. 3. Packing diagram of (I) showing C—H-Cg  $\pi$  intermolecular interactions.

### 3.2. Hirshfeld Surface Analysis

A new way of looking at intermolecular interactions in molecular crystals, and one that is fundamentally different from conventional methods of crystal structure analysis, using the Hirshfeld surfaces to partition crystal space. The red spots on the Hirshfeld surface indicate the presence of close contacts, whereas areas without close contacts are shown as blue spots. [46-48]. The Hirshfeld surface of complex (I), mapped over the  $d_{norm}$  range from  $-0.2858$  to  $1.6287$  Å, which are shown as transparent to allow visualization of the asymmetric unit of the given crystal structure is represented in Figure 4. The shape index that is the most sensitive to very little changes in surface, gives the information about each donor-acceptor pair. The C—H...Cg  $\pi$  contacts in the compound represented by the concave red triangles above the plane of the [Mg(TTP)(DMAP)<sub>2</sub>] molecule and the contacts by ring atoms of molecule inside these surfaces represent by convex blue triangles (Figure 5-b). The curvedness is a measure of ‘how much shape’, which usually tends to divide the surface into patches, which indicates interactions between neighboring molecules. Therefore, sharp curvature regions of the surface correspond to high curvedness values, while the flat regions correspond to low curvedness values. The relatively large green regions, observed as flat patches in the curvedness mapped surfaces, indicate the presence of  $\pi$ - $\pi$  interactions between molecules (Figure 5-c) which is confirmed by the PLATON calculations (see crystallographic section) [49].

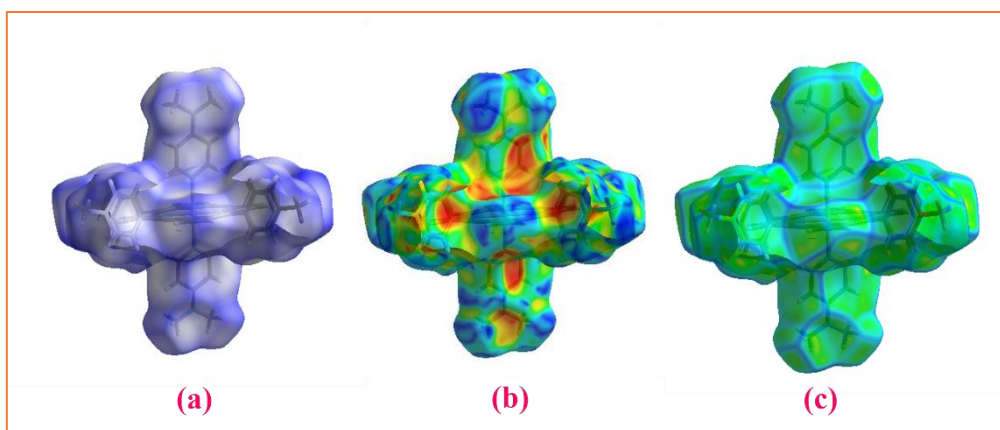


Fig. 4. (a): Hirshfeld surface mapped with  $d_{norm}$ , (b): Shape index and (c): Curvedness of complex (I)

The 2D fingerprints plots ( $d_i$  versus  $d_e$ ) along with the corresponding Hirshfeld surface of (I) (Figure 5) presents intermolecular contacts between atoms and shows the percentage of contributions from different interaction types. The H...H contacts (63.3%), the C...H/H...C, the N...H/H...N interactions comprised 14.4%, and 1% of the HS, respectively.

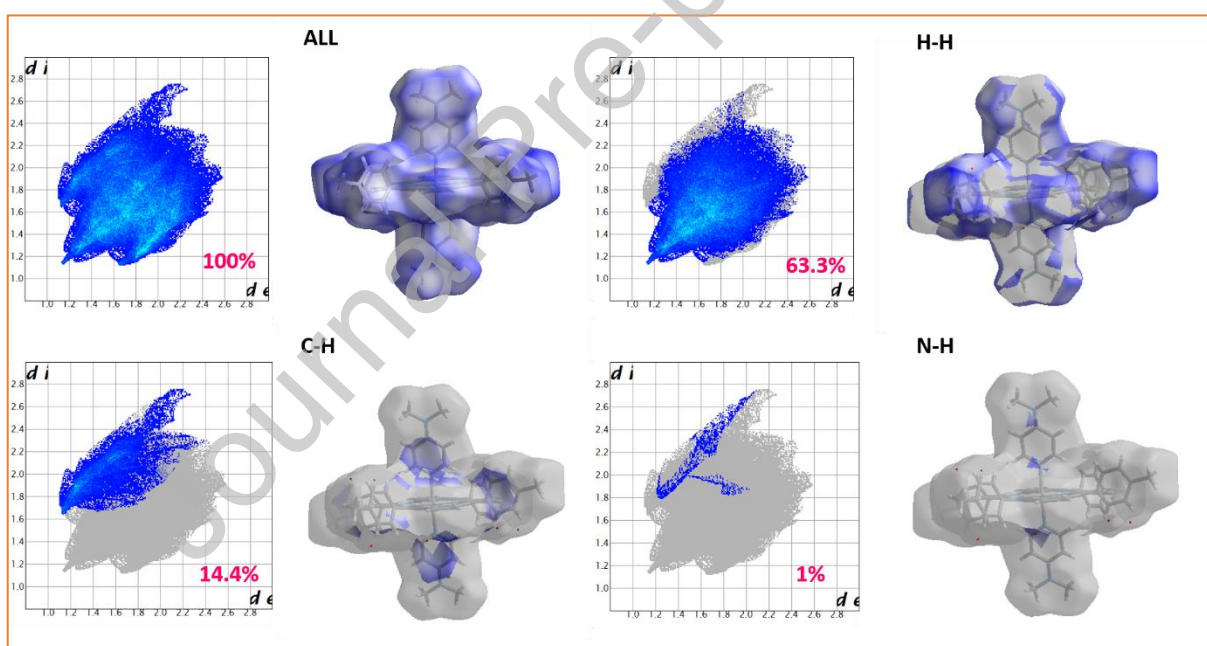


Fig. 5. Hirshfeld surface mapped over  $d_{norm}$  and decomposed fingerprint plots for the dominant interactions in complex (I).

### 3.3. Proton NMR spectroscopy

$^1\text{H}$  NMR experimental and theoretical data ( $\delta$  in ppm) of  $\text{H}_2\text{TTP}$ ,  $[\text{Mg}^{\text{II}}(\text{TTP})]$  and complex (I) in  $\text{CDCl}_3$  solvent were gathered in Table S2. Gauge including atomic orbital (GIAO)  $^1\text{H}$  chemical shift calculation of the title compounds was calculated at B3LYP-D3/6-311 G (d, p)

and compared to the experimental Data. The  $^1\text{H}$  chemical shift values were reported in ppm using tetramethylsilane (TMS  $\delta = 0.00$  ppm) as the common internal standard [50].  $^1\text{H}$  NMR spectral analysis was carried out in  $\text{CDCl}_3$  to investigate the structures of our compound. The  $^1\text{H}$  NMR spectrum of the  $\text{H}_2\text{TTP}$  free base porphyrin presents NH pyrrole protons very shielded appear at  $-2.74$  ppm (Figure S3) and  $-3.08$  ppm for the experimental and the theoretical results, respectively. These signals disappear when the porphyrin is metallated with Mg(II) (Figures S4). For the  $\text{H}_2\text{TTP}$ , the corresponding metallated porphyrins [ $\text{Mg}(\text{TTP})$ ] and [ $\text{Mg}(\text{TTP})(\text{DMAP})_2$ ] complexes, the  $\beta$ -pyrrolic protons and the aromatic protons of the *meso*-phenyl rings of the TTP moiety resonate in the range  $8.88 - 8.10$  ppm for the experimental data and in the range  $8.91 - 8.07$  ppm for the theoretical data, indicating a diamagnetic character for all three species (Figures S4 and S5). Furthermore, the chemical shift values of the  $\text{N}(\text{CH}_3)_2$  protons ( $\text{H}_{\text{a}}$ ), the *ortho* ( $\text{H}_{\text{L,o}}$ ) and the *meta* ( $\text{H}_{\text{L,m}}$ ) protons of the DMAP axial ligand of (**I**) are  $7.67$ ,  $7.25$  and  $2.70$  ppm, respectively. We notice a small diminishing of the resolution of the spectra which is probably caused by the ultrafast ripping process in solution [51].

### 3.4. FT-IR investigation

The comparative observed and computed vibrational wavenumbers in gas phase are listed in Table 3. The simulated harmonic vibrational wavenumbers were scaled down uniformly by a factor of  $0.967$  for B3LYP-D3/6-311 G(d, p) level of theory, which accounts for systematic errors caused by basis set incompleteness, neglect of electron correlation and vibrational anharmonicity [40,52]. Figure S6 shows the experimental FT-IR spectra with the calculated IR spectra of all compounds. The  $\nu(\text{C-H})$  stretching frequency of the  $\text{H}_2\text{TTP}$  free base is in the range  $[2900-2973 \text{ cm}^{-1}]$  and  $[2905-3047 \text{ cm}^{-1}]$  for the experimental and the theoretical values, respectively. The values of the  $\nu(\text{N-H})$  stretching frequency deduced from the experimental and the theoretical spectra of  $\text{H}_2\text{TTP}$  are in the range  $[3300-3340] \text{ cm}^{-1}$  and at  $3450 \text{ cm}^{-1}$ , respectively. On the other hand, the absorption bands, attributed to the  $\delta(\text{CCH})$  bending mode of the  $\text{H}_2\text{TTP}$  moiety is observed at  $966 \text{ cm}^{-1}$ . For complex (**I**), the DMAP axial ligand exhibits an absorption band attributed to the  $\nu(\text{CH})$  stretching at  $3025 \text{ cm}^{-1}$  and the theoretical  $\nu(\text{CH})$  stretching frequency value of this axial ligand is  $3063 \text{ cm}^{-1}$ . In Table 3 one can notice the good agreement between the experimental and theoretical FT-IR data of complex (**I**).

Table 3. Observed and calculated FT-IR spectra of H<sub>2</sub>TTP, [Mg (TTP)] and (I).

$\nu$ (cm <sup>-1</sup> )	H <sub>2</sub> TTP			[Mg(TTP)]			(I)		
	$\nu_{\text{Exp}}$	$\nu_{\text{Theo}}$ unscaled	$\nu_{\text{Theo}}$ scaled <sup>a</sup>	$\nu_{\text{Exp}}$	$\nu_{\text{Theo}}$ unscaled	$\nu_{\text{Theo}}$ scaled <sup>a</sup>	$\nu_{\text{Exp}}$	$\nu_{\text{Theo}}$ unscaled	$\nu_{\text{Theo}}$ scaled <sup>a</sup>
$\nu(\text{NH-pyrrol})$	3300-3340	3568	3450	-	-	-	-	-	3450
$\nu(\text{CH-porph})$	2900-2973	3026-3196	2926-3090	2900-2973	3035-3196	2934-3090	2808-2920	3005-3152	2905-3047
$\nu(\text{CCH porph})$	966	992	966	997	1025	991	996	1023	989
$\nu(\text{CH-DMAP})$	-	-	-	-	-	-	3025	3168	3063

<sup>a</sup> Obtained from the wave numbers calculated at B3LYP-D3/6-311 G (d, p) using scaling factors 0.967.

### 3.5. Fluorescence studies

The experimental emission spectra of H<sub>2</sub>TTP, [Mg(TTP)] and [Mg(TTP)(DMAP)<sub>2</sub>] $\cdot$ 2CH<sub>2</sub>Cl<sub>2</sub> (I) are recorded at room temperature with concentrations  $\sim 10^{-6}$  M under an excitation wavelength of 450 nm. The theoretical emission spectra for the title compounds have been computed using TDDFT/CAM-B3LYP-D3 method in dichloromethane solvent with 6-311 G (d, p) basis sets. The  $\lambda_{\text{max}}$  values of the Q(0,0) and Q(0,1) bands, the fluorescence quantum yields ( $\phi_f$ ) and the fluorescence lifetimes ( $\tau_f$ ) of our three porphyrin compounds and a selection of *meso*-arylporphyrins and Mg(II) metalloporphyrins are summarized in Table S3. The spectra showed an important blue shift of [Q(0,0) (41 nm) and the Q(0,1) (66 nm)] and [Q(0,0) (38 nm) and the Q(0,1) (57 nm)] for the experimental and theoretical bands, respectively, due to the metalation of the H<sub>2</sub>TTP porphyrin with Mg(II) metal. The coordination of the DMAP ligand to the magnesium(II) center metal of [Mg(TTP)] has a minor effect on the positions of the Q bands (Figure 6, Table S3) and there is a weak charge transfer from [Mg(TTP)] to the DMAP axial ligand. This result complies well with the theoretical emission results.



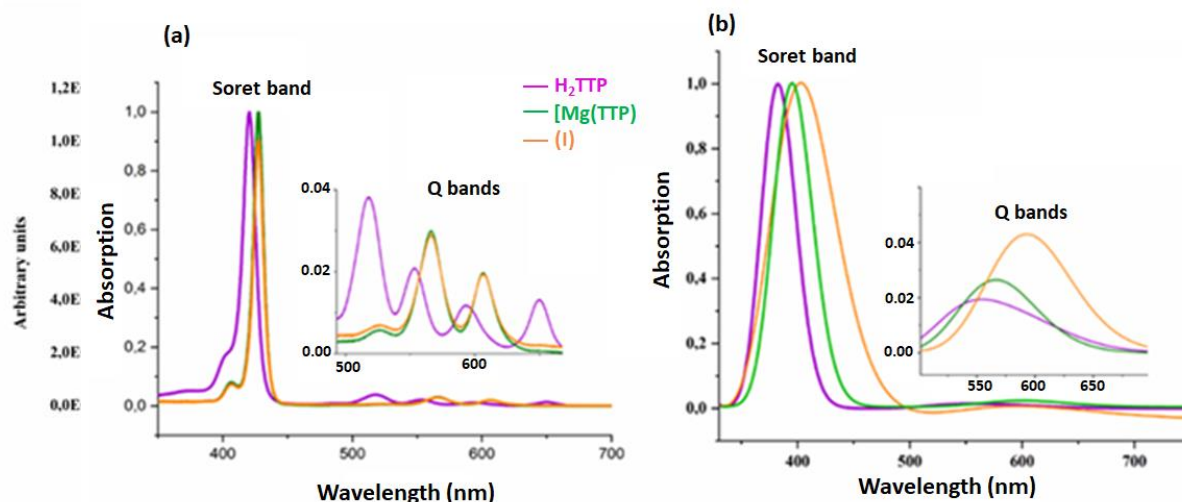


Fig. 6. Experimental and theoretical emission spectra of H<sub>2</sub>TTP, [Mg(TTP)] and complex (I) in dichloromethane ( $\sim 10^{-6}$  M).

The fluorescence quantum yields ( $\Phi_f$ ) and the fluorescence lifetimes ( $\tau_f$ ) values of the H<sub>2</sub>TTP free base porphyrin are  $\sim 10\%$  and 7.90 ns, respectively which are in the normal range of *meso*-porphyrins [53, 54]. These values increase after metalation of H<sub>2</sub>TTP by Mg(II) leading to [Mg(TTP)] and complex (I) with  $\Phi_f$  and  $\tau_f$  values of 15%/13% and 9.10/5.0 ns, respectively.

### 3.6. UV/Vis spectrometry

The four orbital model proposed by Gouterman [55] shows that porphyrins and metalloporphyrins display two kinds of absorption bands. The strongest, in the near UV region, known as the Soret Band (or B band), and weaker absorption Q bands in the visible region. Figure 7 illustrates the experimental and theoretical UV/Vis spectra in dichloromethane at room temperature of H<sub>2</sub>TTP, [Mg(TTP)] and [Mg(TTP)(4-DMAP)<sub>2</sub>] $\cdot 2\text{CH}_2\text{Cl}_2$  (I). The simulated spectra of these three porphyrinic species were calculated at TD-DFT approach with CAM-B3LYP-D3/6-311 G (d, p) in dichloromethane solvent. The H<sub>2</sub>TTP exhibits a Soret band at 420 nm and at 382 nm for the experimental and theoretical spectra, respectively, corresponding to the allowed transition between the S<sub>0</sub> ground state to the second excited state S<sub>2</sub> (S<sub>0</sub>  $\rightarrow$  S<sub>2</sub>) and four Q bands at 518, 552, 593 and 649 nm corresponding to the S<sub>0</sub>  $\rightarrow$  S<sub>1</sub> transition where S<sub>1</sub> is the first excited state.



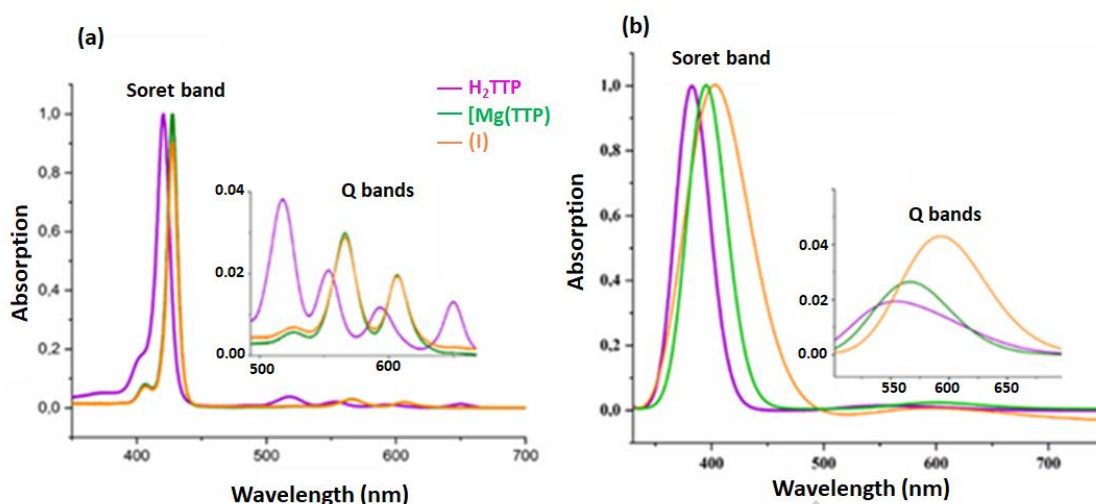


Fig. 7. Experimental (a) and calculated (b) UV/Vis spectra of H<sub>2</sub>TTP, [Mg(TTP)] and **I** in CH<sub>2</sub>Cl<sub>2</sub>.

The metallated [Mg(TTP)] complex and complex (**I**) present Soret bands redshifted compared to that of the H<sub>2</sub>TTP free base porphyrin with values of 427 and 397 nm for the experimental and the theoretical spectra, respectively (Table S4). By comparing the experimental and the calculated spectra of the (**I**), we notice (i) that for the theoretical spectrum the presence of a Soret band at 397 nm which is redshifted compared to that of the experimental spectrum and (ii) the Q bands of the theoretical spectrum are present as a single broad and very weak band (Table S4). This is due to the theoretical studies which cannot deal with some factors such as hydrogen bonding and solvent effect with sufficient accuracy like the practical study.

### 3.7. Electrospray ionization Mass Spectrometry analysis

The ESI-HRMS mass spectrum depicted in Figure S7 confirms that two DMAP ligands are present in the coordination environment of the magnesium atom of complex (**I**) in dichloromethane solution. The experimental and the theoretical  $m/z$  values of the [Mg(TTP)(DMAP)<sub>2</sub>]<sup>+</sup> fragment are 937.4551 and 937.4556, respectively. The ESI-MS in positive ion mode confirms the presence of the [Mg(TTP)]<sup>+</sup> (theoretical value of  $m/z$  is 692.27) by the presence of peak at a  $m/z$  692.2782 and [Mg(TTP)(DMAP)<sub>2</sub>+H]<sup>+</sup> by the presence of peak at  $m/z$  937.4547.

### 3.8. Cyclic voltammetry

Figure 8 presents the cyclic voltammogram of the  $[\text{Mg}(\text{TTP})(\text{DMAP})_2] \cdot \text{CH}_2\text{Cl}_2$  (**I**) with tetra-*n*-butylammonium perchlorate (TBAP) as the supporting electrolyte (0.2 M) in the dichloromethane under argon atmosphere. The electrochemical data for our TTP-Mg-DMAP complex along with those for other related species are given in Table 4.

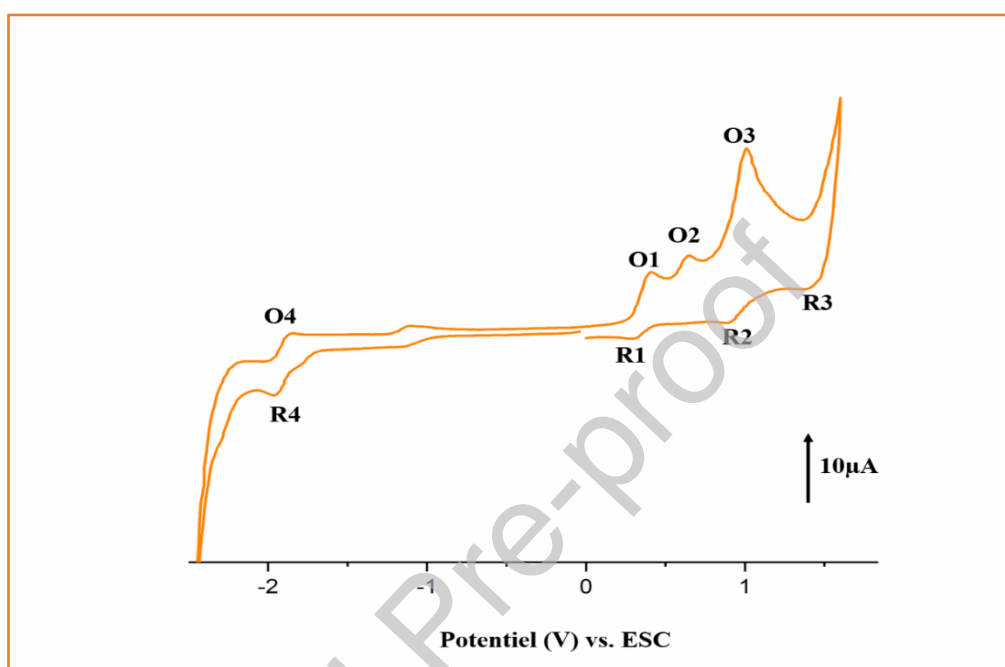
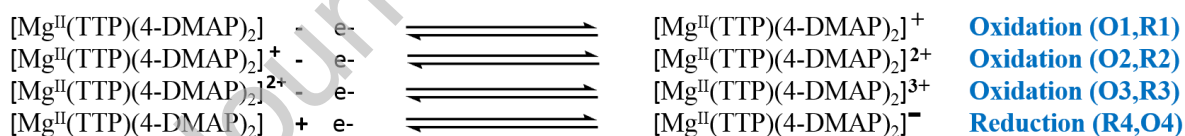


Fig. 8. Cyclic voltammogram of (**I**). The solvent is  $\text{CH}_2\text{Cl}_2$ , and the concentration is ca.  $10^{-3}$  M in 0.2 M TBAP, 50 mV/s, vitreous carbon working electrode ( $\varnothing = 3$  mm).



Scheme 1: Oxidation and reduction reactions of complex **I**

Metalloporphyrins with non-electroactive divalent metal ions such as Zn(II), Cd(II) and Mg(II) present usually two or three reversible one electron oxidations and one or two electron reductions of the porphyrin macrocycle [62,63]. For our synthetic Mg-TTP-DMAP derivative (**I**), the cyclic voltammogram shows three one-electron reversible oxidation waves with half-potential ( $E_{1/2}$ ) values of 0.61 (O1,R1), 0.91 (O2,R2) and 1.22 (O3,R3) V, respectively and a one-electron reversible reduction wave with  $E_{1/2}$  value of -1.42 V (Figure 8, Table 4, Scheme

1). Therefore, the electrochemical response of (**I**) is characteristic of metalloporphyrins with a non-electroactive central metal ion.

Table 4. Cyclic voltammetry data for (**I**) and a selection of *meso*-arylphenylporphyrin species.

Compound	Ring oxidation			Ring reduction	Ref.
	First Oxid. (O1, R1)	Second Oxid (O2, R2)	Third oxid. (O3, R3)	First Red. (R4, O4)	
	$E_{1/2}^b$	$E_{1/2}$	$E_{1/2}$	$E_{1/2}$	
<i>Meso-arylporphyrins</i>					
H <sub>2</sub> TPP <sup>c</sup>	1.02	1.26	-	-1.20	[56]
H <sub>2</sub> TPBP <sup>d</sup>	0.95	1.36	1.48	-1.12	[57]
H <sub>2</sub> TMPP <sup>e</sup>	1.02	1.19	1.67	-1.19	[58]
H <sub>2</sub> TCIPP	1.00	1.23	1.53	-1.09	[58]
<i>Magnesium(II)-meso-arylporphyrins</i>					
[Mg(TFP)(THF) <sub>2</sub> ] <sup>f,g</sup>	0.68	-	-	-1.40	[59]
[Mg(TPP)(HMTA) <sub>2</sub> ] <sup>h</sup>	0.73	0.99	-	-1.45	[60]
{[[Mg(TPP)(pyz)]] <sub>n</sub> } <sup>i</sup>	0.65	0.95	-	-1.65	[61]
[Mg(TTP)(DMAP) <sub>2</sub> ]·2CH <sub>2</sub> Cl <sub>2</sub> ( <b>I</b> )	0.65	1.05	1.32	-1.61	tw

<sup>a</sup>:  $E_{1/2}$  = half wave potential, <sup>c</sup>: H<sub>2</sub>TPP = *meso*-tetraphenylporphyrin, <sup>d</sup>: H<sub>2</sub>TPBP = *meso* tetrakis [4(benzoyloxy)phenyl]porphyrin, <sup>e</sup>: H<sub>2</sub>TMPP = *meso*-tetra(*para*-methoxyphenyl)porphyrin, <sup>f</sup>: THF = tetrahydrofuran, <sup>g</sup>: TFP = *meso*-furylporphyrin, <sup>h</sup>: HTMA = Hexamethylenetetramine, <sup>i</sup>: pyz = pyrazine

### 3.9. Frontier molecular orbital analysis

The highest occupied molecular orbital (HOMO) and the lowest unoccupied molecular orbital (LUMO) are named as frontier molecular orbitals (FMOs) and they are a very important parameter for quantum chemistry. These calculations are a very useful method to indicate the eventual charge transfer interaction within a molecule. The values of the energies of the HOMO and LUMO orbitals serve to exemplify the kinetic stability of a molecule and its chemical reactivity. All these electronic and quantum chemical parameters of the title compound were calculated at the CAM-B3LYP-D3 method using 6-311 G (d, p) basis sets in the dichloromethane solvent and they were listed in Table S5.

3D plots of the HOMO and LUMO orbitals are shown in Figure 9 where the positive and

negative phases are represented in red and green color, respectively. The HOMO and LUMO are localized on different parts of the molecules. As shown in Figure 9, for the HOMO orbital (MO-bonding orbital) of H<sub>2</sub>TTP (Figure 9-a), the charge density is mostly localized on the nitrogen atoms and the *meso carbons* and in the  $\alpha$  and  $\beta$  positions of alternative pyrrole rings. For the LUMO orbital (MO-antibonding orbital) of H<sub>2</sub>TTP, the density is mostly located in the 24 atoms porphyrin core. Concerning the [Mg(TTP)] (Figure 9-b) and [Mg(TTP)(DMAP)<sub>2</sub>] (Figure 9-c) the charge density of the HOMO and the LUMO orbitals are mainly located on the porphyrin macrocycle.

The energy gap of HOMO-LUMO is an important value which serves as a stability index. It should be indicated that the change in band gap brings about variations in conductivity. The relationship between conductivity and energy band gap (E<sub>g</sub>) can be estimated using the following equation:

$$\sigma \propto -\exp(-E_g/K_B.T) \quad (7)$$

where,  $\sigma$  is the electric conductivity and  $K_B$  denotes the Boltzmann constant. It is conspicuous that a small decrease in the band gap results in a significantly higher electrical conductivity.

Furthermore, a large HOMO-LUMO gap indicates a high molecular stability in the sense of its lower reactivity in chemical reactions [25,29].

In our case, the HOMO-LUMO energy gap is slightly increased after metallation of the porphyrin with Mg(II), from 2.684 eV for H<sub>2</sub>TTP to 2.690 eV for [Mg(TTP)]. Then, it decreases to 2.526 eV for complex (I), after the coordination with the dimethylaminopyridine (DMAP) axial ligand. It implies that [Mg(TTP)(DMAP)<sub>2</sub>] becomes more conductive (with lower molecular stability and high reactivity in chemical reactions) compared to H<sub>2</sub>TTP and [Mg(TTP)].

Conceptual DFT based descriptors have been used to get a better idea of the structure of molecules and their reactivity by computing the chemical potential ( $\mu$ ), global hardness ( $\eta$ ) and softness ( $\sigma$ ).

The chemical potential ( $\mu$ ) characterizes the escaping tendency of electrons from a stable system. The chemical hardness ( $\eta$ ) measures the resistance of a molecule to a charge transfer while the softness ( $\sigma$ ) is the capacitance of a molecule to acquire charge. As shown in Table S5, the [Mg(TTP)(DMAP)<sub>2</sub>] presents low chemical potential ( $\mu$ ) and chemical hardness ( $\eta$ ), which are 2.831 eV and 1.276 eV respectively. However, it has a higher reactivity than H<sub>2</sub>TTP and [Mg(TTP)]. Moreover, the softness is a good indicator of the chemical stability of a molecule.

We notice that  $[\text{Mg}(\text{TTP})(\text{DMAP})_2]$  is the softest. Whereas the Gap energy of  $[\text{Mg}(\text{TTP})]$ , which is 2.690 eV, is higher than those of  $\text{H}_2\text{TTP}$  and  $[\text{Mg}(\text{TTP})(\text{DMAP})_2]\cdot 2\text{CH}_2\text{Cl}_2$  indicating that  $[\text{Mg}(\text{TTP})]$  is the hardest molecule. Consequently, we may conclude that after the complexation with the axial ligand,  $[\text{Mg}(\text{TTP})(\text{DMAP})_2]\cdot 2\text{CH}_2\text{Cl}_2$  becomes more polarizable than  $\text{H}_2\text{TTP}$  and  $[\text{Mg}(\text{TTP})]$  respectively, because they need small energy to be excited. These results explain the eventual charge transfer interaction within the molecule.  $\text{H}_2\text{TTP}$ ,  $[\text{Mg}(\text{TTP})]$  and  $[\text{Mg}(\text{TTP})(\text{DMAP})_2]\cdot 2\text{CH}_2\text{Cl}_2$  (**I**)

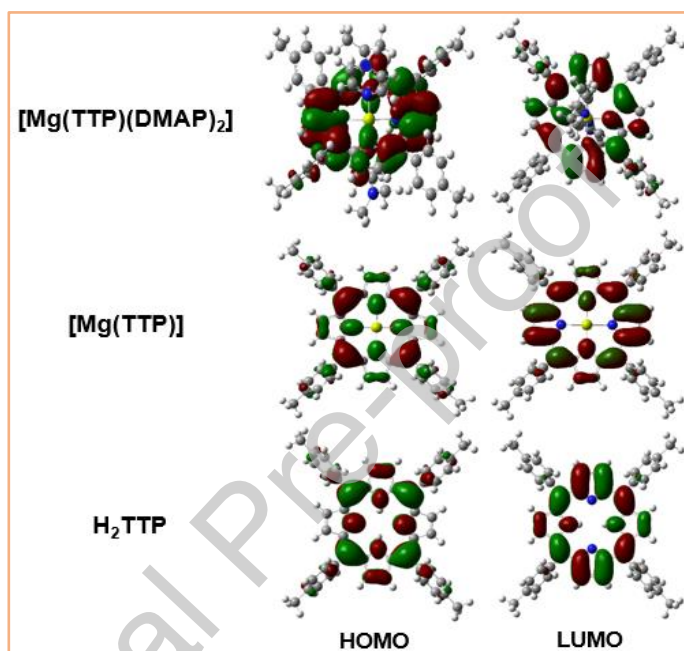


Fig. 9. Representative frontier orbitals of  $\text{H}_2\text{TTP}$ ,  $[\text{Mg}(\text{TTP})]$  and  $[\text{Mg}(\text{TTP})(\text{DMAP})_2]\cdot 2\text{CH}_2\text{Cl}_2$  (**I**) calculated at CAM-B3LYP-D3/6-311 G (d, p) method.

## 4. Antifungal activity

### 4.1. Antidermatophyte activity

The  $\text{H}_2\text{TTP}$  free base porphyrin and complexes  $[\text{Mg}(\text{TTP})]$  and  $[\text{Mg}(\text{TTP})(\text{DMAP})_2]\cdot 2\text{CH}_2\text{Cl}_2$  (**I**) were evaluated for their *in vitro* antifungal activity against five pathogenic fungi three yeasts strains (*C. albicans* ATCC90028, *C. glabrata* (ATCC 64677) and *C. tropicalis* (ATCC 66029) and two dermatophytes' strains (*trichophyton rubrum* (MS 7793.1 and *Microsporum canis* (MS 8972)). We first tested our porphyrin derivatives against *candida* spp. Anticandidal activities of the porphyrin species were determined by microdilution method by determining MIC and MFC values. MIC and MFC values are given in the Table 5.  $[\text{Mg}(\text{TTP})(\text{DMAP})_2]\cdot 2\text{CH}_2\text{Cl}_2$  (**I**) showed the best activity against all the three strains of *Candida* spp. *C. albicans*, *C. glabrata*

and *C. tropicalis* with MIC values in the range of 2.5 mg.mL<sup>-1</sup> to 10 µg.mL<sup>-1</sup>. This species presents a fungicidal potential with MIC values between 5 and >10 mg.mL<sup>-1</sup>

A lower antifungal potential was observed for H<sub>2</sub>TTP free porphyrin and [Mg(TTP)], which presented fungistatic concentrations (MIC) values starting from 5 mg mL<sup>-1</sup> and fungicidal yields (MFC) almost higher than 10 mg.L<sup>-1</sup> against the three *Candida* species.

Table 5. Minimum inhibitory concentration (MIC) and minimum fungicidal concentration (MFC) of H<sub>2</sub>TTP, [Mg(TTP)] and [Mg(TTP)(DMAP)<sub>2</sub>]<sup>-1</sup>·2CH<sub>2</sub>Cl<sub>2</sub> (**I**) porphyrin derivatives against yeasts strains.

Porphyrin compound	<i>Candida albicans</i> (ATCC 90028)		<i>Candida glabrata</i> (ATCC 64677)		<i>Candida tropicalis</i> (ATCC 66029)	
	MIC (mg.L <sup>-1</sup> )	MFC (mg.L <sup>-1</sup> )	MIC (mg.L <sup>-1</sup> )	MFC (mg.L <sup>-1</sup> )	MIC (mg.L <sup>-1</sup> )	MFC (mg.L <sup>-1</sup> )
H <sub>2</sub> TTP	>10	>10	5	>10	5	5
[Mg(TTP)]	>10	>10	>10	>10	>10	>10
[Mg(TTP)(DMAP) <sub>2</sub> ] <sup>-1</sup> ·2CH <sub>2</sub> Cl <sub>2</sub> ( <b>I</b> )	>10	>10	2.5	10	10	10

The screening of the susceptibility of *M. canis* and *T. rubrum* clinical strains to H<sub>2</sub>TTP, [Mg(TTP)] and (**I**) show different results (Figure 10). The results of the screening indicate that (**I**) have a significantly increasing inhibitory potential for both *M. canis* and *T. rubrum*, with percentages of inhibition 64.07 % and 25%, respectively, and this with an initial concentration of 10 mg.mL<sup>-1</sup>. In contrast, both [Mg(TTP)] and the free porphyrin exhibit weaker antidermatophytic effects, with percentage of inhibition values ranging from 11.11% to 16%. The negative control (10% DMSO) showed no antidermatophytic activity. As a consequence of these promising results, the [Mg(TTP)] and [Mg(TTP)(DMAP)<sub>2</sub>]<sup>-1</sup>·2CH<sub>2</sub>Cl<sub>2</sub> (**I**) complexes were selected for further experiment to determine the corresponding MIC.

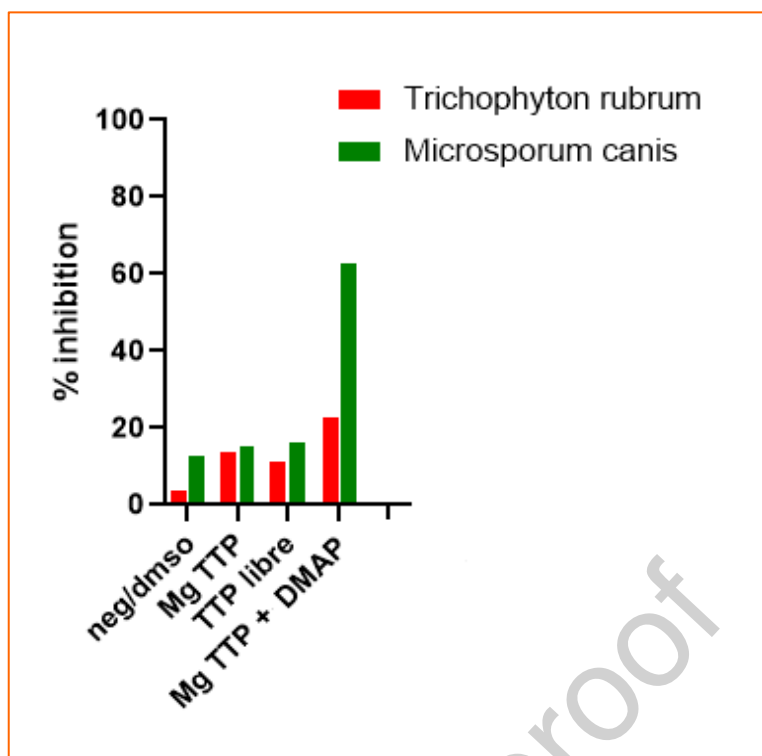


Fig. 10. Screening anti-dermatophytic activities of the three porphyrinic compounds.

In an attempt to estimate MIC values, increasing concentrations of  $1.25 \text{ mg.mL}^{-1}$ ,  $2.5 \text{ mg.mL}^{-1}$  and  $5 \text{ mg.mL}^{-1}$  were tested. The percentages of inhibition of the tested strains by  $[\text{Mg}(\text{TTP})]$  and  $[\text{Mg}(\text{TTP})(\text{DMAP})_2] \cdot 2\text{CH}_2\text{Cl}_2$  (**I**) are shown in Figure 11. We noticed that these two metalloporphyrins inhibit the growth of dermatophytes mycelia in a dose-dependent manner. Indeed, each increase in porphyrin concentrations increased the inhibition of the fungal strains. At a concentration of  $5 \text{ mg.mL}^{-1}$ ,  $[\text{Mg}(\text{TTP})]$  and  $[\text{Mg}(\text{TTP})(\text{DMAP})_2] \cdot 2\text{CH}_2\text{Cl}_2$  (**I**) inhibited the mycelial growth of *T. rubrum* (69.41%), and *M. canis* (53.38%). The inhibition decreased over the days until it reached the percentage of 47.35% (*T. rubrum*) and 23.13% (*M. canis*) at the 5 mg concentration, 44.11% (*T. rubrum*) and 5.08% (*M. canis*) at the  $2.5 \text{ mg.mL}^{-1}$  concentration and 19.85 % (*T. rubrum*) and 5.56 % (*M. canis*) for the  $1.25 \text{ mg.mL}^{-1}$  concentration.

According to these results, increasing the concentration of  $[\text{Mg}(\text{TTP})]$  and  $[\text{Mg}(\text{TTP})(\text{DMAP})_2] \cdot 2\text{CH}_2\text{Cl}_2$  (**I**) remarkably increases the inhibition (Figure 11).

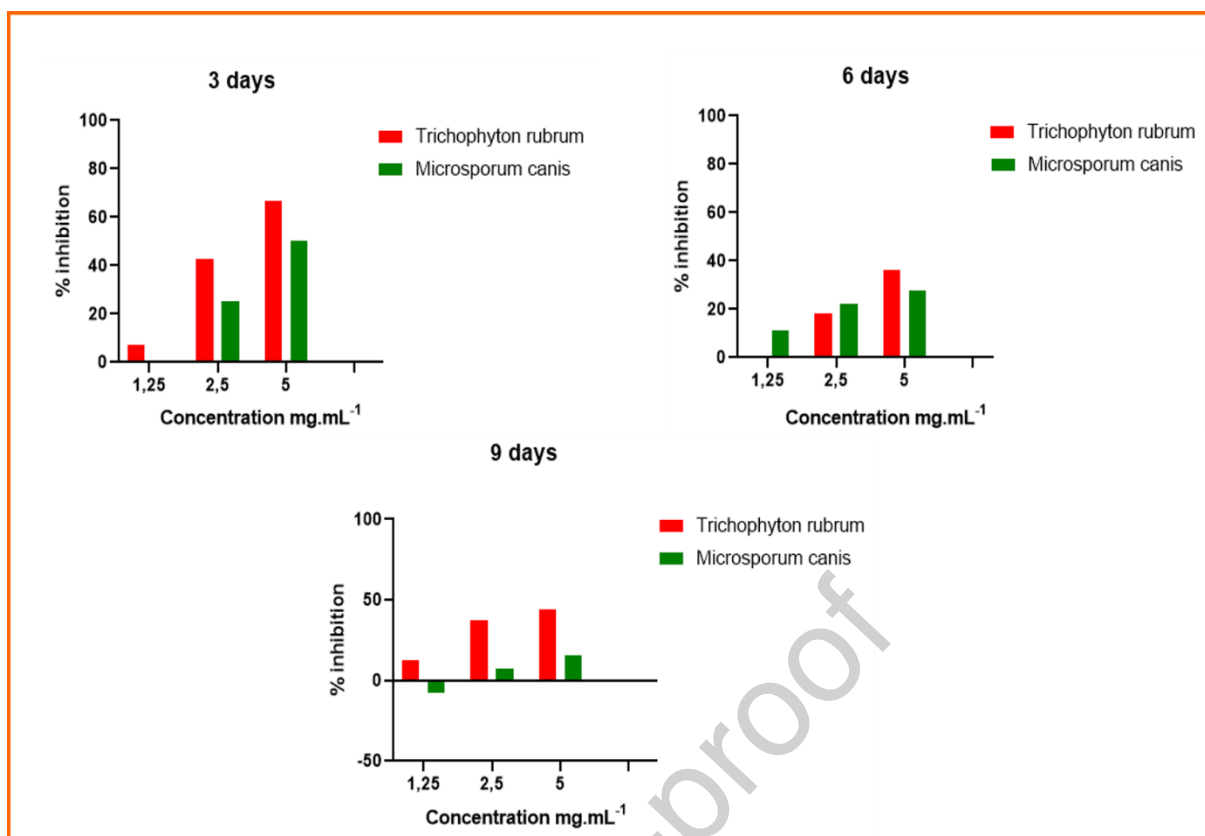


Fig. 11 Anti-dermatophytes activity of  $[\text{Mg}(\text{TTP})]$  and  $[\text{Mg}(\text{TTP})(\text{DMAP})_2] \cdot 2\text{CH}_2\text{Cl}_2$  (**I**).

## 5. Conclusion

In conclusion, in the present work we described the synthesis of the two  $\text{H}_2\text{TTP}$  and  $[\text{Mg}(\text{TTP})]$  starting materials and a new six-coordinated magnesium(II) bis(4-dimethylaminopyridine) complex with the *meso*-tetra(*para*-tolylphenyl)porphyrin ( $\text{H}_2\text{TTP}$ ) with the formula  $[\text{Mg}(\text{TTP})(\text{DMAP})_2] \cdot 2\text{CH}_2\text{Cl}_2$  (**I**). This later coordination compound was characterized by single crystal X-ray diffraction which shows that the magnesium central metal is hexacoordinated by the four nitrogen atoms of the TTP macrocycle and the nitrogen atoms of the two trans DMAP axial ligands. The crystal packing is stabilized by C–H $\cdots$ Cl and by C–H $\cdots$  $\pi$  intermolecular interactions. Hirshfeld surface analyses and two-dimensional fingerprint plots were used to quantify the intermolecular interactions present in the crystal. The spectroscopic and photophysical properties of (**I**) were studied experimentally and theoretically. DFT calculations have been optimized using B3LYP-D3/6-311 G (d, p). High resolution Electrospray Ionization Mass Spectrometry (ESI- HRMS) shows the presence of the



[Mg(TTP)(DMAP)<sub>2</sub>+H]<sup>+</sup> fragment in dichloromethane solvent. The biological studies reveal that the three tested porphyrinic species could be classified as antifungal agents. Indeed, [Mg(TTP)] and [Mg(TTP)(DMAP)<sub>2</sub>] $\cdot$ 2CH<sub>2</sub>Cl<sub>2</sub> present a high sensibility against *C. glabrata* (ATCC 64677) with CMI= 2.5mg/L and an increasing inhibition against two genus of dermatophytes.

conflict of interest

None

#### AUTHOR CONTRIBUTIONS

**Souhir Jabli:** Data curation-Lead, Software-Lead, Writing-original draft-Lead

**Marwa Chaabene:** Investigation-Lead, Software-Lead, Writing-original draft-Lead

**Thierry Roisnel:** Data curation-Supporting, Software-Lead

**Florian Molton :** Formal analysis-Lead, Resources-Lead

**Frédérique Loiseau:** Formal analysis-Lead, Resources-Lead

**Philippe Jehan:** Funding acquisition-Lead, Validation-Lead

**Rafik Ben Chaâbane:** Methodology-Lead, Validation-Lead

**Habib Nasri:** Project administration-Lead, Methodology-Lead

#### References

- [1] A.D. Adler, F.R. Longo, J.D. Finarelli, J. Goldmacher, J. Assour, L. Korsakoff, A simplified synthesis for meso-tetraphenylporphine, *J. Org. Chem.* 32 (1967) 476–476.
- [2] J.P. Collman, R.R. Gagne, C. Reed, T.R. Halbert, G. Lang, W.T. Robinson, Picket fence porphyrins. Synthetic models for oxygen binding hemoproteins, *J. Am. Chem. Soc.* 97 (1975) 1427–1439
- [3] T. Birnbaum, T. Hahn, C. Martin, J. Kortus, M. Fronk, F. Lungwitz, D.R.T. Zahn, G. Salvan, Optical and magneto-optical properties of metal phthalocyanine and metal porphyrin thin films, *J. Phys. Condens. Matter.* 26 (2014) 104-201.
- [4] A.E. O'Connor, W.M. Gallagher, A.T. Byrne, Porphyrin and Nonporphyrin Photosensitizers in Oncology: Preclinical and Clinical Advances in Photodynamic Therapy, *Photochem. Photobiol.* 85 (2009) 1053–1074.

- [5] V.K. Gupta, D.K. Chauhan, V.K. Saini, S. Agarwal, M.M. Antonijevic, H. Lang, A Porphyrin Based Potentiometric Sensor for Zn<sup>2+</sup> Determination, *Sensors*. 3 (2003) 223–235.
- [6] N. Kobayashi, P. Janda, A.B.P. Lever, Cathodic reduction of oxygen and hydrogen peroxide at cobalt and iron crowned phthalocyanines adsorbed on highly oriented pyrolytic graphite electrodes, *Inorg. Chem.* 31 (1992) 5172–5177.
- [7] C.M. Drain, A. Varotto, I. Radivojevic, Self-Organized Porphyrinic Materials, *Chem. Rev.* 109 (2009) 1630–1658.
- [8] E.G. Girichev, M.I. Bazanov, N.Z. Mamardashvili, A. Gjezjak, Electrochemical and Electrocatalytical Properties of 3,7,13,17-Tetramethyl-2,8,12,18-Tetrabutylporphyrin in Alkaline Solution, *Molecules*. 5 (2000) 767–774.
- [9] W.A. Nevin, G.A. Chamberlain, Photovoltaic properties of iodine-doped magnesium tetraphenylporphyrin sandwich cells. II. Properties of illuminated cells, *J. Appl. Phys.* 69 (1991) 4324–4332.
- [10] A.E. O'Connor, W.M. Gallagher, A.T. Byrne, Porphyrin and Nonporphyrin Photosensitizers in Oncology: Preclinical and Clinical Advances in Photodynamic Therapy, *Photochem. Photobiol.* 85 (2009) 1053–1074.
- [11] B.B. Beyene, A.M. Mihirteu, M.T. Ayana, A.W. Yibeltal, Synthesis, characterization and antibacterial activity of metalloporphyrins: Role of central metal ion, *Results Phys.* 2 (2020) 100073.
- [12] R. Elashnikov, M. Radocha, I. Panov, S. Rimpelova, P. Ulbrich, A. Michalcova, V. Svorcik, O. Lyutakov, Porphyrin-silver nanoparticles hybrids: Synthesis, characterization and antibacterial activity, *Mater. Sci. Eng. C*. 102 (2019) 192–199.
- [13] M.V. Tesakova, V.I. Parfenyuk, The Electrochemical Evaluation of the Antioxidant Activity of Substituted Tetraphenylporphyrins, *Russ J Electrochem.* 53 (2017) 1281–1285.
- [14] C. Cui, Q. Wang, Q. Liu, X. Deng, T. Liu, D. Li, X. Zhang, Porphyrin-based porous organic framework: An efficient and stable peroxidase-mimicking nanozyme for detection of H<sub>2</sub>O<sub>2</sub> and evaluation of antioxidant, *Sens. Actuators B Chem.* 277 (2018) 86–94.
- [15] U. Singh, A.M. Malla, I.A. Bhat, A. Ahmad, M.N. Bukhari, S. Bhat, S. Anayutullah, A.A. Hashmi, Synthesis, molecular docking and evaluation of antifungal activity of Ni(II), Co(II) and Cu(II) complexes of porphyrin core macromolecular ligand, *Microb. Pathog.* 93 (2016) 172–179.

- [16] S. Moghnie, A. Tovmasyan, J. Craik, I. Batinic-Haberle, L. Benov, Cationic amphiphilic Zn-porphyrin with high antifungal photodynamic potency, *Photochem. Photobiol. Sci.* 16 (2017) 1709–1716.
- [17] A. N. Vzorov, D. W. Dixon, J. S. Trommel, L. G. Marzilli, R. W. Compans, *Antimicrob. Agents and Chemother.* 46 (2002) 3917-3925.
- [18] V. Car, O. Gaud, I. Sylvain, O. Bow-don, M. Spiro, J. Blais, R. Granet, P. Kraus, M. Guilloton, *J. Photochem. Photobiol. B : Biol.* 48 (1999) 57.
- [19] N. Amiri, F.B. Taheur, S. Chevreux, E. Wenger, G. Lemerrier, H. Nasri, Synthesis, crystal structure and spectroscopic characterizations of porphyrin-based Mg(II) complexes – Potential application as antibacterial agent, *Tetrahedron.* 73 (2017) 7011–7016.
- [20] N. Amiri, M. Hajji, F.B. Taheur, S. Chevreux, T. Roisnel, G. Lemerrier, H. Nasri, Two novel magnesium (II) meso-tetraphenylporphyrin-based coordination complexes: Syntheses, combined experimental and theoretical structures elucidation, spectroscopy, photophysical properties and antibacterial activity, *J. Solid State Chem.* 258 (2018) 477–484.
- [21] A.A. Jarzęcki, P.M. Kozłowski, P. Pulay, B.-H. Ye, X.-Y. Li, Scaled quantum mechanical and experimental vibrational spectra of magnesium and zinc porphyrins, *Spectrochimica Acta Part A: Molecular and Biomolecular Spectroscopy.* 53 (1997) 1195–1209.
- [22] Gaussian 09 Citation | Gaussian.com, (n.d.). <https://gaussian.com/g09citation/> (accessed December 19, 2020).
- [23] A.D. Adler, F.R. Longo, J.D. Finarelli, J. Goldmacher, J. Assour, L. Korsakoff, A simplified synthesis for meso-tetraphenylporphine, *J. Org. Chem.* 32 (1967) 476–476.
- [24] R. Timkovich, A. Tulinsky, Structure of aquomagnesium tetraphenylporphyrin, *J. Am. Chem. Soc.* 91 (1969) 4430–4432. <https://doi.org/10.1021/ja01044a018>.
- [25] R. Weiss, J. Fischer, V. Bulach, V. Schünemann, M. Gerdan, A.X. Trautwein, J.A. Shelnut, C.P. Gros, A. Tabard, R. Guilard, *Inorg. Chim. Acta* 337 (2002) 223–232,
- [26] A. Ghosh, S.M. Mobin, R. Frohlich, R.J. Butcher, D.K. Maity, M. Ravikanth, *Inorg. Chem.* 49 (2010) 8287–8297.
- [27] SMART, SAINT, and SADABS, Bruker AXS Inc., (2008), Madison, WI, USA.
- [28] A. Altomare, G. Casciarano, C. Giacovazzo, A. Guagliardi, M.C. Burla, G. Polidori, M. Camalli, SIRPOW.92 – A program for automatic solution of crystal structures by direct methods optimized for powder data, *Journal of Applied Crystallography* 27 (1994) 435–436.
- [29] G.M. Sheldrick, Crystal structure refinement with SHELXL, *Acta Cryst C* 71 (2015) 3–8.
- [30] A.L. Spek, PLATON SQUEEZE: a tool for the calculation of the disordered solvent contribution to the calculated structure factors, *Acta Crystallogr C Struct Chem* 71 (2015) 9-18

- [31] C.F. Macrae, I.J. Bruno, J.A. Chisholm, P.R. Edgington, P. McCabe, E. Pidcock, L. Rodriguez-Monge, R. Taylor, J. van de Streek, P.A. Wood, Mercury CSD 2.0 – new features for the visualization and investigation of crystal structures, *J Appl Cryst.* 41 (2008) 466–470.
- [32] A.D. Becke, Density-functional thermochemistry. III. *The Journal of Chemical Physics.* 98 (1993) 5648–5652.
- [33] S. Grimme, J. Antony, S. Ehrlich, H. Krieg, *The Journal of Chemical Physics*, 132 (2010) 154104.
- [34] J.G. Małecki, Synthesis, crystal, molecular and electronic structures of thiocyanate ruthenium complexes with pyridine and its derivatives as ligands, *Polyhedron.* 29 (2010) 1973–1979.
- [35] G. Wang, Y. Lu, C. Zhou, Y. Zhang, *Acta Cryst.* 65 (2009) 1113.
- [36] M. Chaabene, G. Bouzid, P. Mignon, R. Chaabane, A.-R. Allouche, New zinc phthalocyanine derivatives for nitrogen dioxide sensors: A theoretical optoelectronic investigation, *Journal of Molecular Graphics and Modelling.* 88 (2019) 174–182.
- [37] S. Agren, M. Chaabene, A. Allouche, R. Ben Chaâbane, M. Lahcinie, M.H.V. Baouab, Blue Highly Fluorescent Boranil Derived From Anil Ligand: Synthesis, Characterization, Experimental and Theoretical Evaluation of Solvent Effect on Structures and Photophysical Properties, *Appl Organomet Chem.* (2020). <https://doi.org/10.1002/aoc.5764>.
- [38] K. Wolinski, J.F. Hinton, P. Pulay, *Journal of the American Chemical Society.* 1990, 112, 8251–8260.
- [39] L. Yang, A.-M. Ren, J.-K. Feng, X.-J. Liu, Y.-G. Ma, M. Zhang, X.-D. Liu, J.-C. Shen, H.-X. Zhang, *J. Phys. Chem. A.* 108 (2004) 6797–6808.
- [40] M. Chaabene, S. Agren, J. Bennagi, A.-R. Allouche, L. Mohamed, R. Chaabane, M. Baouab, Spectroscopic characterization and Binding interaction of heavy metal onto the Surface Receptor of the Azobenzene: DFT and experimental approach, *Journal of Molecular Structure.* 1244 (2021) 130962.
- [41] M. Chaabene, G. Bouzid, S. Raoudha, H. Ghalla, M. Jabli, R. Chaabane, A.-R. Allouche, Insights into theoretical detection of CO<sub>2</sub>, NO, CO, O<sub>2</sub>, and O<sub>3</sub> gases molecules using Zinc phthalocyanine with peripheral mono and tetra quinoleinoxy substituents: Molecular geometries, Electronic properties, and Vibrational analysis, *Chemical Physics.* (2021).
- [42] Gaussian 09, Revision A.02, M. J. Frisch, G. W. Trucks, H. B. Schlegel, G. E. Scuseria, M. A. Robb, J. R. Cheeseman, G. Scalmani, V. Barone, G. A. Petersson, H. Nakatsuji, X. Li, M. Caricato, A. Marenich, J. Bloino, B. G. Janesko, R. Gomperts, B. Mennucci, H. P. Hratchian, J. V. Ortiz, A. F. Izmaylov, J. L. Sonnenberg, D. Williams-Young, F. Ding, F.

Lipparini, F. Egidi, J. Goings, B. Peng, A. Petrone, T. Henderson, D. Ranasinghe, V. G. Zakrzewski, J. Gao, N. Rega, G. Zheng, W. Liang, M. Hada, M. Ehara, K. Toyota, R. Fukuda, J. Hasegawa, M. Ishida, T. Nakajima, Y. Honda, O. Kitao, H. Nakai, T. Vreven, K. Throssell, J. A. Montgomery, Jr., J. E. Peralta, F. Ogliaro, M. Bearpark, J. J. Heyd, E. Brothers, K. N. Kudin, V. N. Staroverov, T. Keith, R. Kobayashi, J. Normand, K. Raghavachari, A. Rendell, J. C. Burant, S. S. Iyengar, J. Tomasi, M. Cossi, J. M. Millam, M. Klene, C. Adamo, R. Cammi, J. W. Ochterski, R. L. Martin, K. Morokuma, O. Farkas, J. B. Foresman, and D. J. Fox, Gaussian, Inc., Wallingford CT. **2016**.

[43] S. Hrichi, R. Chaabane-Banaoues, D. Giuffrida, D. Mangraviti, Y. Oulad El Majdoub, F. Riganod, L. Mondello, H. Babba, Zine Mighri, F. Cacciola, Effect of seasonal variation on the chemical composition and antioxidant and antifungal activities of *Convolvulus althaeoides* L. leaf extracts, *Arab. J. Chem.* 13 (2020) 5651-5668.

[44] V. McKee, C.C. Ong, G.A. Rodley. *Inorg. Chem.* 23 (1984) 4242-4248.

[45] N. Amiri, M. Hajji, T. Roisnel, G. Simonneaux, H. Nasri, Synthesis, molecular structure, photophysical properties and spectroscopic characterization of new 1D-magnesium(II) porphyrin-based coordination polymer, *Res Chem Intermed.* 44 (2018) 5583–5595.

[46] J.J. McKinnon, M.A. Spackman, A.S. Mitchell, *Acta Crystallogr. B* 60 (2004) 627–668.

[47] F.L. Hirshfeld, Bonded-atom fragments for describing molecular charge densities, *Theoret. Chim. Acta.* 44 (1977) 129–138.

[48] M.A. Spackman, P.G. Byrom, A novel definition of a molecule in a crystal, *Chem. Phys. Lett.* 267 (1997) 215–220.

[49] J.J. McKinnon, M.A. Spackman, A.S. Mitchell, Novel tools for visualizing and exploring intermolecular interactions in molecular crystals, *Acta Cryst B.* 60 (2004) 627–668.

[50] C.D.A. León, G.A. Echeverría, O.E. Piro, S.E. Ulic, J.L. Jios, J.A. Pereañez, I.C.H. Castañeda, H. Pérez, The role of non-covalent interactions in some 2-trifluoromethylchromones in the solid state, *New J. Chem.* 41 (2017) 14659–14674.

[51] M. Chaabene, S. Agren, A.-R. Allouche, M. Lahcinie, R.B. Chaâbane, M.H.V. Baouab, Theoretical and experimental investigations of complexation with  $\text{BF}_3 \cdot \text{Et}_2\text{O}$  effects on electronic structures, energies and photophysical properties of Anil and tetraphenyl (hydroxyl) imidazol, *Applied Organometallic Chemistry.* 33 (2019) 5218.

[52] NIST Computational Chemistry Comparison and Benchmark Database, NIST Standard Reference Database Number 101, Release 19, April 2018, Editor: Russell D. Johnson III, <http://cccbdb.nist.gov/>.

- [53] K. Ezzayani, A. Ben Khelifa, F. Ben Taheur, M. Guergueb, A. Mansour, J. -C. Daran, H. Nasri, Effect of the coordination of  $\pi$ -acceptor 4-cyanopyridine ligand on the structural and electronic properties of meso-tetra(para-methoxy) and meso-tetra(para-chlorophenyl) porphyrin cobalt(II) coordination compounds. Application in the catalytic degradation of methylene blue dye, *Inorg. Chim. Acta* 514 (2021) 119960.
- [54] K. Ezzayani, A. Ben Khelifa, E. Saint-Aman, F. Loiseau, H. Nasri, Complex of hexamethylenetetramine with magnesium-tetraphenylporphyrin : Synthesis, structure, spectroscopic characterizations and electrochemical properties, *J. Mol. Struct.* 1137 (2017) 412-418.
- [55] M. Gouterman, in: D. Dolphin (Ed.), *The Porphyrins*, vol. III, Academic Press, New York, 1978.
- [56] S.J. Bonyhady, C. Jones, S. Nembenna, A. Stasch, A.J. Edwards, G.J. McIntyre,  $\beta$ -Diketimate-Stabilized Magnesium(I) Dimers and Magnesium(II) Hydride Complexes: Synthesis, Characterization, Adduct Formation, and Reactivity Studies, *Chem. Eur. J.* 16 (2010) 938–955.
- [57] S. Nasri, I. Zahou, I. Turowska-Tyrk, T. Roisnel, F. Loiseau, E. Saint-Amant, H. Nasri, Synthesis, Electronic Spectroscopy, Cyclic Voltammetry, Photophysics, Electrical Properties and X-ray Molecular Structures of meso-Tetrakis[4-(benzoyloxy)phenyl]porphyrinatozinc(II) Complexes with Aza Ligands, *Eur. J. Inorg. Chem.* (2016) 5004–5019.
- [58] M. Guergueb, S. Nasri, J. Brahmi, F. Loiseau, F. Molton, T. Roisnel, V. Guerineau, I. Turowska-Tyrk, K. Aouadi, H. Nasri, Effect of the coordination of  $\pi$ -acceptor 4-cyanopyridine ligand on the structural and electronic properties of meso -tetra( para -methoxy) and meso -tetra( para-chlorophenyl) porphyrin cobalt( ii ) coordination compounds. Application in the catalytic degradation of methylene blue dye, *RSC Adv.* 10 (2020) 6900–6918.
- [59] A. Ghosh, S.M. Mobin, R. Fröhlich, R.J. Butcher, D.K. Maity, M. Ravikanth, Effect of Five Membered Versus Six Membered Meso-Substituents on Structure and Electronic Properties of Mg(II) Porphyrins: A Combined Experimental and Theoretical Study, *Inorg. Chem.* 49 (2010) 8287–8297.
- [60] K. Ezzayani, A. Ben Khelifa, E. Saint-Aman, F. Loiseau, H. Nasri, Complex of hexamethylenetetramine with magnesium-tetraphenylporphyrin: Synthesis, structure, spectroscopic characterizations, and electrochemical properties, *J. Mol. Struct.* 1137 (2017) 412–418.
- [61] A.B. Khelifa, K. Ezzayani, M. Guergueb, F. Loiseau, E. Saint-Aman, H. Nasri, Synthesis, molecular structure, spectroscopic characterization and antibacterial activity of the pyrazine magnesium porphyrin coordination polymer, *J. Mol. Struct.* 1227 (2021) 129508.

[62] K. Ezzayani, Z. Denden, S. Najmudin, C. Bonifácio, E. Saint-Aman, F. Loiseau, H. Nasri, Exploring the Effects of Axial Pseudohalide Ligands on the Photophysical and Cyclic Voltammetry Properties and Molecular Structures of MgII Tetraphenylporphyrin Complexes, *Eur. J. Inorg. Chem.* 2014 (2014) 5348–5361.

[63] C.C. Ong, V. McKee, G.A. Rodley, The crystal and molecular structure of a monohydrated dipicoline magnesium tetraphenylporphyrin complex, *Inorg. Chim. Acta* 123 (1986) L11–L14.

Journal Pre-proof